RSC Advances

PAPER

View Article Online
View Journal | View Issue

Check for updates

Cite this: *RSC Adv.*, 2017, **7**, 20206

Temperature-dependence studies of organolead halide perovskite-based metal/semiconductor/metal photodetectors†

Yucheng Wang,[a] Yuming Zhang,[a] Yintao Liu,[a] Tiqiang Pang,[a] Ziyang Hu,*[b] Yuejin Zhu,[b] Suzhen Luan[a] and Renxu Jia *[a]

Received 6th February 2017
Accepted 3rd April 2017

DOI: 10.1039/c7ra01496a

rsc.li/rsc-advances

In this paper, polycrystalline perovskite ($CH_3NH_3PbI_xCl_{3-x}$) photodetectors with a structure of Au/$CH_3NH_3PbI_xCl_{3-x}$/Au are prepared and are shown to have good performance. The measured electrical parameters demonstrate that the current behavior of the perovskite photodetectors is dependent of work temperature from 300 K to 350 K. We find that only space charge limited conduction mechanism fits the current–voltage (*I–V*) curves under small external voltage (0.1–0.7 V) both under darkness and illumination. The lattice vibration scattering plays the major role in the dark, leading to a decreased current as the temperature increases under the same external voltage, and an enlarged current increasing with the temperature is due to the leading role of the ionized impurity scattering. At each temperature, the rising slope of the *I–V* curves decrease with the increase of voltage both under dark and illumination. The values of on/off ratio, responsivity and detectivity increase with the measured temperature, which indicates that the polycrystalline perovskite photodetector can work with better performance at high temperature. However, the stability in the dark gradually becomes weak as the temperature increases, especially at 330 K and above.

Open Access Article. Published on 07 April 2017. Downloaded on 2/13/2026 10:51:31 AM.
This article is licensed under a Creative Commons Attribution 3.0 Unported Licence.

1. Introduction

Recently, hybrid organic–inorganic lead halide perovskites ($CH_3NH_3PbX_3$, where X = Cl, Br, and I) have attracted great attention as light absorbers not only for frequently studied solar cells[1–10] but also for (LEDs),[11–13] field-effect transistors (FETs),[14–16] lasers,[17–19] and photodetectors.[20–30] The perovskites have excellent semiconductor properties, such as a direct band gap, a broad absorption range and high carrier mobility.[23,24] Until now, there are several research works reported on Metal–Semiconductor–Metal (MSM) photodetectors based on Si or GaAs,[31–34] and several significant efforts to fabricate high performance $CH_3NH_3PbX_3$ photodetectors have been made: Makhsud I. *et al.* produced a light detector showing high gain-bandwidth product using large perovskite single crystals,[20] Hao Lu *et al.* made the first all perovskite self-powered nanosystem by integrating a solar perovskite with a perovskite photodetector,[23] and Z. Lian *et al.* reported a lowest detectable irradiance power density of 2.12 nW cm^{-2}, with the highest responsivity of 953 A W^{-1} and external quantum efficiency of 2.22×10^5%.[24] These high property perovskite photodetectors are prepared with several structures, like Au/perovskites/Au,[24,28] Pt/Ti/perovskites/Pt/Ti,[26] ITO/perovskites/ITO,[27] and the solar cell structures.[25,29] Basic electrical parameters such as on/off ratio, responsivity and detectivity are measured under different illumination intensities[23,24,27] and optical wavelength.[26,27] Although so many remarkable efforts have been made to detect the characteristics of photodetectors based on $CH_3NH_3PbX_3$ single crystals under different structures and conditions, polycrystalline perovskites photodetectors are rarely discussed, which should be considered owing to their low preparation cost. In addition, temperature-dependence studies are significant for the performance and reliability of the photodetectors, which should be focused on by researchers.

In this work, several Au/$CH_3NH_3PbI_xCl_{3-x}$/Au photodetectors are prepared and measured. X-ray diffraction (XRD), photoluminescence spectroscopy (PL), and Scanning Electron Microscope (SEM) are given to detect the quality of the perovskite film. Key parameters like on/off ratio, responsivity, detectivity, rise time and fall time are calculated. For detail analysis of the temperature-dependence studies, the electrical parameters are measured under different temperatures vary from 300 K to 350 K (perovskites are considered to decompose at higher temperature). Several current mechanisms are fitted to explain the strange phenomenon of *I–V* curves.

[a]*School of Microelectronics, Xidian University, Key Laboratory of Wide Band-Gap Semiconductor Materials and Devices, Xi'an 710071, China. E-mail: rxjia@mail.xidian.edu.cn*

[b]*Department of Microelectronic Science and Engineering, Ningbo Collaborative Innovation Center of Nonlinear Hazard System of Ocean and Atmosphere, Ningbo University, Ningbo, 315211, China. E-mail: huziyang@nbu.edu.cn*

† Electronic supplementary information (ESI) available: See supplementary material for the current mechanisms of the studied photodetectors. See DOI: 10.1039/c7ra01496a

This journal is © The Royal Society of Chemistry 2017

Open Access Article. Published on 07 April 2017. Downloaded on 2/13/2026 10:51:31 AM.
This article is licensed under a Creative Commons Attribution 3.0 Unported Licence.

2. Experimental

400 μm Al_2O_3 was employed as the insulating substrate, and a pair of interdigitated Au-film electrodes (2000 μm long and 250 μm wide for each one) were deposited on the substrate, which have 34 fingers and the same interspacing distance of 150 μm. Methylammonium iodide (CH_3NH_3I) and lead chloride ($PbCl_2$) were prepared according to previous work.[26] The preheated precursor solution at 70 °C was used for fabricating the $MAPbI_{3-x}Cl_x$ thin film. Next, the $CH_3NH_3PbI_{3-x}Cl_x$ precursor solution was spin coated onto the treated substrate at a rate of 4000 rpm for 30 s. The wet perovskite film was then annealed on a hot plate to complete the crystallization. The photodetector with a structure of Au/$CH_3NH_3PbI_{3-x}Cl_x$/Au/Al_2O_3 was completed and shown in Fig. 1(a).

The diffraction patterns of the $CH_3NH_3PbI_{3-x}Cl_x$ films were detected by XRD measurements (New D8-Advance, Cu Kα). The steady-state PL measurements were acquired using a fluorescence spectrometer (Horiba FluoroMax®-4) with an excitation wavelength of 460 nm. The surfaces of the PVK films were prepared by SEM (JEOL JSM-6701F). Current–voltage (*I–V*) measurements were analyzed under different temperatures (300 K, 310 K, 320 K, 330 K, 340 K, and 350 K) and different illumination intensity (dark and 10 mW cm^{-2}) with $\lambda = 550$ nm (Keysight B1500A semiconductor parameter analyzer). A solar simulator (xenon lamp, Oriel, AM 1.5G light) and optical attenuators were used for adjustable illumination. The transient photocurrent response was performed under a 550 nm pulse light from a light-emitting diode.

3. Results and discussion

The smooth perovskite film was illustrated by SEM in Fig. 1(b), proving that the polycrystalline PVK film is ideal for device application. Fig. 1(c) gives the XRD measurements of the crystallized perovskite thin film, which strong peaks at 14.08°, 28.41°, and 43.19° can be assigned to (110), (220), and (330) diffractions of $CH_3NH_3PbI_3$, respectively. PL data of PVK film in Fig. 1(d) indicated a strong bandgap photoluminescence centered at 770 nm. Fig. 2(a) gives the typical current–voltage (*I–V*) curves of the perovskite photodetector in the dark and under 10 mW cm^{-2} illumination intensity, the voltage was swept in the sequence 0 → 10 V → 0 V (forward) and 0 → −10 V → 0 V (reverse). Several key parameters are calculated by eqn (1) and (2). On/off ratio is the ratio of photocurrent (I_{ph}) to dark current (I_d), responsivity (R) indicates how efficiently the detector responds to an optical signal, and L_{light} is the incident light power, which is the product of illumination intensity and illumination area (9.9×10^{-6} m^2). For the detectivity (D), q is the elementary charge, and I_d is the dark current density when the dark current is dominated by the shot noise.[26] The device performance plotted against external bias are illustrated in Fig. 2(b), R is not given in the figure (about 10^{-2} A W^{-1}) as R is proportional to the current under the same light power. The highest detectivity (3×10^{12} jones) and highest on/off ratio (77) are shown in Fig. 2(b), indicating a good performance photodetector.

$$R = \frac{I_{ph}}{L_{light}} \quad (1)$$

$$D = \frac{I_{ph}/L_{light}}{(2qI_d)^{0.5}} \quad (2)$$

Fig. 2(a) and (b) illustrates the changed current of the photodetector under dark and light illumination. The on/off

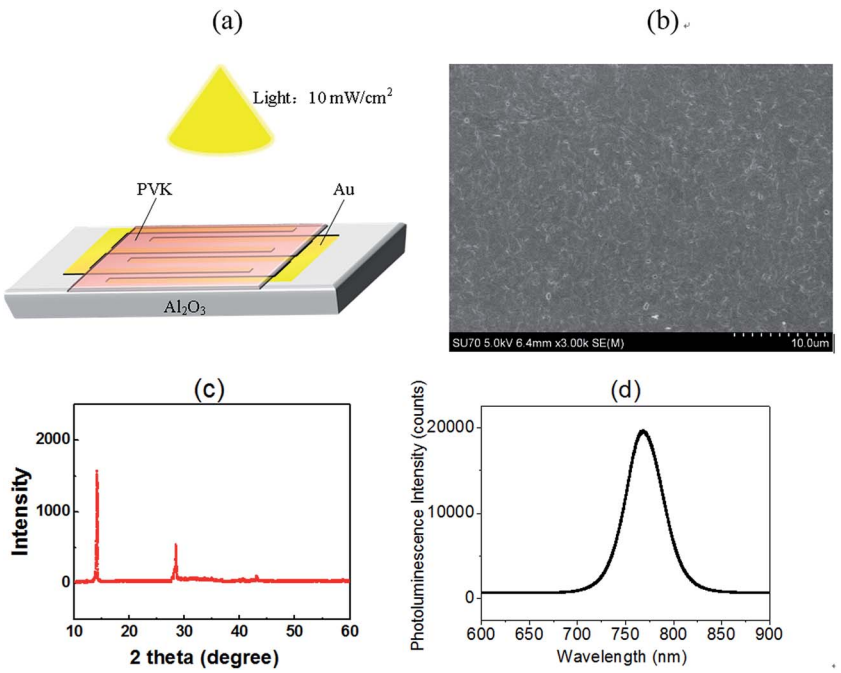

Fig. 1 (a) Photodetector with a structure of Au/$CH_3NH_3PbI_{3-x}Cl_x$/Au, (b) FE-SEM images of crystallized $CH_3NH_3PbI_{3-x}Cl_x$ film, (c) XRD data from crystallized $CH_3NH_3PbI_{3-x}Cl_x$ film, (d) photoluminescence spectroscopy (PL) spectrum of $CH_3NH_3PbI_{3-x}Cl_x$ film.

Open Access Article. Published on 07 April 2017. Downloaded on 2/13/2026 10:51:31 AM.
This article is licensed under a Creative Commons Attribution 3.0 Unported Licence.

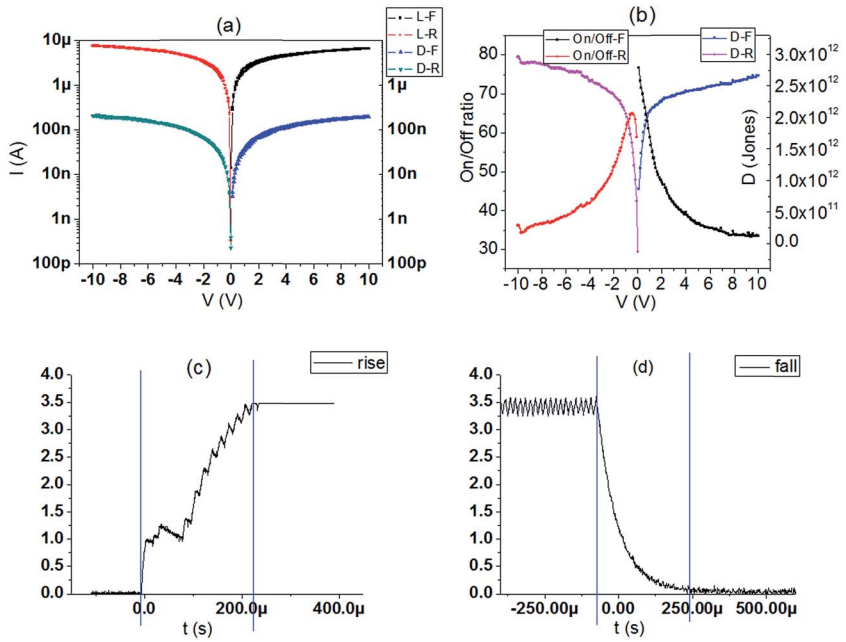

Fig. 2 (a) Current–voltage (I–V) curves of the perovskite photodetector in the dark and under 10 mW cm^{-2} illumination intensity, L: light D: dark F: forward R: reverse (b) on/off ratio and detectivity (D) plotted against external bias. (c) Rise time and (d) fall time of photocurrent during switching of light illumination.

ratio is increased with the reduced applied voltage. Herein, the rise time and fall time of the photodetector are defined as the time taken for the 10% to increase to 90% of the peak value. The rise time (180 μs) and fall time (150 μs) are calculated by Fig. 2(c) and (d). The fast response of the device is promising for large-area photodetector applications. Temperature-dependence is a quite significant property for device application. I–V curves of the perovskite photodetector under temperatures vary from 300 K to 350 K are illustrated in Fig. 3(a) and (b). Strange phenomenon is observed that the photocurrent rises and the dark current falls as the temperature increases. For each temperature, the rising slope of the I–V curve decreases with the increase of voltage.

Several current mechanisms are applied to explain the phenomenon: space charge limited conduction (SCLC), Poole Frankel conduction (P–F), Fowler Nordheim tunneling (F–N tunneling).[35,36] The definition and fitting formula are given in ESI.† We found only SCLC mechanism fits the I–V curves under small external voltage (0.1–0.7 V) both under dark and illumination as shown in Fig. 3(c) and (d), indicating that the I–V curves fit ohmic characteristics when low voltage is applied. F–N tunneling and P–F mechanisms are not suitable here, seen in Fig. S1.†

Here we consider the scattering mechanism should be responsible for the phenomenon in Fig. 2. There are two main carrier scattering mechanisms: ionized impurity scattering and lattice vibration scattering. Relationships between current and carrier scattering are shown in eqn (3)–(5).

$$I = AnqμE\left(\frac{1}{1/\mu_i + 1/\mu_l}\right) \quad (3)$$

$$\mu_i \propto N_i^{-1} T^{3/2} \quad (4)$$

$$\mu_l \propto T^{3/2} \quad (5)$$

where A is area, n is the concentration of carriers, q is carrier charge, μ is mobility, E is electrical field, μ_i is the mobility governed by ionized impurity scattering, μ_l is the mobility governed by lattice vibration scattering, N_i is concentration of the ionized impurity, and T is the temperature. The lattice vibration scattering plays the major role in the dark where the concentration of carriers is quite low. The current will decrease as the temperature increases under the same applied voltage without illumination. As photo-induced carriers enlarge n in eqn (3), the current increases drastically under illumination compare to that in the dark, and the leading role of scattering mechanism changes to the ionized impurity scattering, which means the current will enlarge with the increase of the temperature under the same external voltage. As for each temperature (in the dark and under light), the rising slope of the I–V curve decreases with the increase of voltage. This is because the concentration of carriers will not increase under the same light illumination power, and the product of electrical field and the mobility will gradually approach to the limit. The value of current will reach 15 μA as the product of electrical field and the mobility will gradually approach to the limit (seen in Fig. S2†), proving the conclusion above. The whole current mechanisms based on different applied voltage are summarized and given in Fig. 4(a).

The organic–inorganic metal halide perovskite is said to be very unstable, especially under high temperature for a long time. Hence, the effect of temperature on the stability and performance of perovskite-based photodetector as a function of operation time (0, 5, 10, and 30 min) is given in Fig. S3(a)–(l).† The photodetector under illumination shows stable properties even after 350 K heat

 This journal is © The Royal Society of Chemistry 2017

Open Access Article. Published on 07 April 2017. Downloaded on 2/13/2026 10:51:31 AM.
This article is licensed under a Creative Commons Attribution 3.0 Unported Licence.

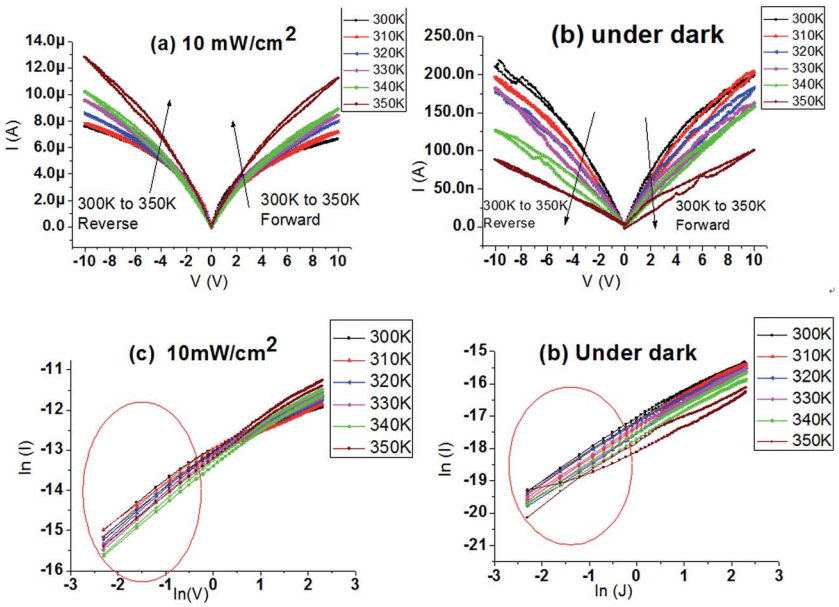

Fig. 3 I–V curves of the perovskite photodetector as a function of temperature from 300 K to 350 K (a) under illumination of 10 mW cm^{-2}, (b) in the dark. F: forward R: reverse. SCLC mechanism fitting curves at temperatures vary from 300 K to 350 K (c) under illumination of 10 mW cm^{-2}, (d) in the dark.

treatment of 30 min. However, the stability in the dark gradually becomes week as the temperature increases. The XRD spectra and UV-Vis spectra of perovskite layer at different temperatures are provided in Fig. S4(a) and (b).† PbI_2 is seen due to the partial thermal decomposition of the perovskite when the temperature climbs to 330 K and above, but the absorption curves under each temperature show nearly no changes. Key parameters like on/off ratio and detectivity of the perovskite photodetectors are calculated and illustrated in Fig. 4(b) and (c). Responsivity is proportional to the photocurrent. It is obvious that the on/off ratio,

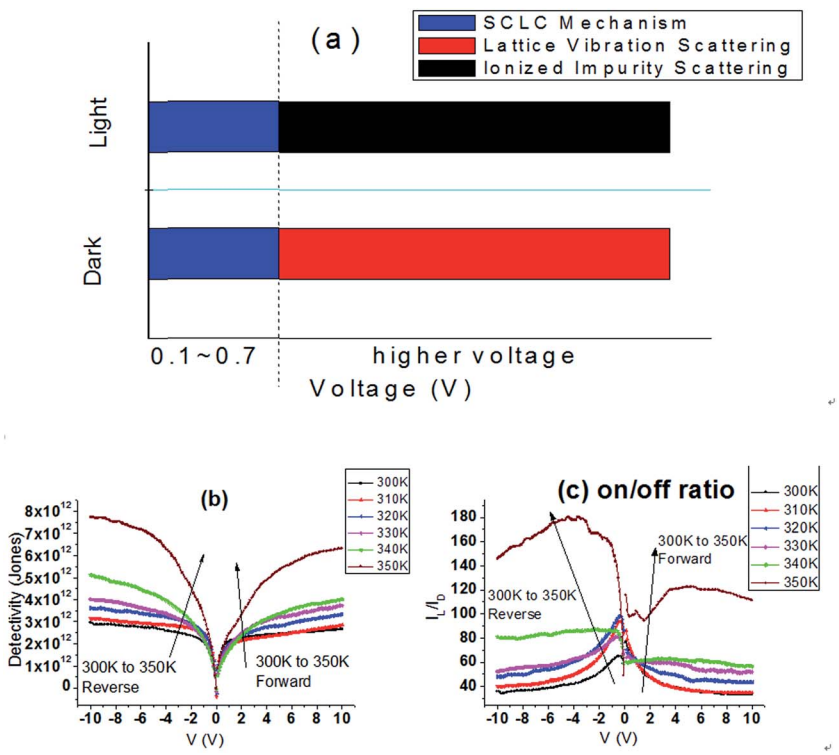

Fig. 4 (a) Current mechanisms based on different applied voltage, (b) detectivity and (c) on/off ratio plotted against external bias under temperatures vary from 300 K to 350 K, F: forward R: reverse.

responsivity and detectivity increase as the temperature increase, which indicates that the perovskite photodetector can gain better performance at high temperature (300 K to 350 K). But when considering the stability by operating for 30 min or more, the performance under high temperature (340–350 K) may be reduced by the jumping dark current.

4. Conclusions

In this work, the polycrystalline perovskite film was applied to fabricate photodetectors, suggesting an ideal material for device application. Key parameters like on/off ratio, responsivity, detectivity, rise time and fall time are calculated, proving that the photodetectors are in good performance. For a detail analysis of the temperature-dependence studies, the photodetectors based perovskites demonstrate different current curves at different temperatures. Under small external voltage, SCLC mechanism fits well the dark and illumination *I–V* curves. The lattice vibration scattering plays the major role in the dark, leading to the decrease of current as the temperature increases. At each temperature, the rising slope of the *I–V* curve decreases with the increased voltage because the product of electrical field and the mobility will gradually approach to the limit. The effect of temperature on the stability shows that the stability in the dark gradually becomes week as the temperature increases, especially in 330 K and above. The values of on/off ratio, responsivity and detectivity increase with the measured temperature, which indicates that the polycrystalline perovskite photodetector can work with better performance at high temperature. However, the performance under high temperature (340–350 K) may be reduced due to the jumping dark current.

Open Access Article. Published on 07 April 2017. Downloaded on 2/13/2026 10:51:31 AM.
This article is licensed under a Creative Commons Attribution 3.0 Unported Licence.

Acknowledgements

The authors would like to acknowledge the financial support from the National Natural Science Foundation, China (Grant No. 51472196 and No. 61234006).

References

1 C. Zuo, H. J. Bolink, H. Han, J. Huang, D. Cahen and L. Ding, Advances in Perovskite Solar Cells, *Adv. Sci.*, 2016, **3**, 1500324.
2 Z. Zhu, C. C. Chueh, F. Lin and A. K. Jen, Enhanced Ambient Stability of Efficient Perovskite Solar Cells by Employing a Modified Fullerene Cathode Interlayer, *Adv. Sci.*, 2016, **3**, 1600027.
3 W. Zhu, C. Bao, F. Li, X. Zhou, J. Yang, T. Yu and Z. Zou, An efficient planar-heterojunction solar cell based on wide-bandgap $CH_3NH_3PbI_{2.1}Br_{0.9}$ perovskite film for tandem cell application, *Chem. Commun.*, 2016, **52**, 304–307.
4 W. Zhu, C. Bao, F. Li, T. Yu, H. Gao, Y. Yi and Z. Zou, A halide exchange engineering for $CH_3NH_3PbI_{3-x}Br_x$ perovskite solar cells with high performance and stability, *Nano Energy*, 2016, **19**, 17–26.
5 Y. Zhou, M. Yang, O. S. Game, W. Wu, J. Kwun, M. A. Strauss and N. P. Padture, Manipulating Crystallization of Organolead Mixed-Halide Thin Films in Antisolvent Baths for Wide-Bandgap Perovskite Solar Cells, *ACS Appl. Mater. Interfaces*, 2016, **8**, 2232–2237.
6 Z. Zhao, X. Chen, H. Wu, X. Wu and G. Cao, Probing the Photovoltage and Photocurrent in Perovskite Solar Cells with Nanoscale Resolution, *Adv. Funct. Mater.*, 2016, **26**, 3048–3058.
7 Z. Yang, C. C. Chueh, P. W. Liang, M. Crump, F. Lin, Z. Zhu and A. K. Y. Jen, Effects of formamidinium and bromide ion substitution in methylammonium lead triiodide toward high-performance perovskite solar cells, *Nano Energy*, 2016, **22**, 328–337.
8 Q. Xue, G. Chen, M. Liu, J. Xiao, Z. Chen, Z. Hu and H. L. Yip, Improving Film Formation and Photovoltage of Highly Efficient Inverted-Type Perovskite Solar Cells through the Incorporation of New Polymeric Hole Selective Layers, *Adv. Energy Mater.*, 2016, **6**, 1502021.
9 Y. Zhao, J. Wei, H. Li, Y. Yan, W. Zhou, D. Yu and Q. Zhao, A polymer scaffold for self-healing perovskite solar cells, *Nat. Commun.*, 2016, **7**, 10228.
10 Y. Shao, Y. Yuan and J. Huang, Correlation of energy disorder and open-circuit voltage in hybrid perovskite solar cells, *Nat. Energy*, 2016, **1**, 15001.
11 X. Gong, Z. Yang, G. Walters, R. Comin, Z. Ning, E. Beauregard and E. H. Sargent, Highly efficient quantum dot near-infrared light-emitting diodes, *Nat. Photonics*, 2016, **10**, 253–257.
12 H. Cho, S. H. Jeong, M. H. Park, Y. H. Kim, C. Wolf, C. L. Lee and S. H. Im, Overcoming the electroluminescence efficiency limitations of perovskite light-emitting diodes, *Science*, 2015, **350**, 1222–1225.
13 Z. K. Tan, R. S. Moghaddam, M. L. Lai, P. Docampo, R. Higler, F. Deschler and F. Hanusch, Bright light-emitting diodes based on organometal halide perovskite, *Nat. Nanotechnol.*, 2014, **9**, 687–692.
14 X. Y. Chin, D. Cortecchia, J. Yin, A. Bruno and C. Soci, Lead iodide perovskite light-emitting field-effect transistor, *Nat. Commun.*, 2015, **6**, 7383.
15 F. Li, C. Ma, H. Wang, W. Hu, W. Yu, A. D. Sheikh and T. Wu, Ambipolar solution-processed hybrid perovskite phototransistors, *Nat. Commun.*, 2015, **6**, 8238.
16 Y. Wang, Y. Zhang, Y. Lu, W. Xu, H. Mu, C. Chen and Y. B. Cheng, Hybrid Graphene-Perovskite Phototransistors with Ultrahigh Responsivity and Gain, *Adv. Opt. Mater.*, 2015, **3**, 1389–1396.
17 U. Bansode, R. Naphade, O. Game, S. Agarkar and S. Ogale, Hybrid Perovskite Films by a New Variant of Pulsed Excimer Laser Deposition: A Room-Temperature Dry Process, *J. Phys. Chem. C*, 2015, **119**, 9177–9185.
18 S. Chen, K. Roh, J. Lee, W. K. Chong, Y. Lu, N. Mathews and A. Nurmikko, A Photonic Crystal Laser from Solution Based Organo-Lead Iodide Perovskite Thin Film, *ACS Nano*, 2016, **10**, 3959–3967.
19 Z. Gu, K. Wang, W. Sun, J. Li, S. Liu, Q. Song and S. Xiao, Two-Photon Pumped $CH_3NH_3PbBr_3$ Perovskite Microwire Lasers, *Adv. Opt. Mater.*, 2016, **4**, 472–479.
20 M. I. Saidaminov, V. Adinolfi, R. Comin, A. L. Abdelhady, W. Peng, I. Dursun and O. M. Bakr, Planar-integrated

Open Access Article. Published on 07 April 2017. Downloaded on 2/13/2026 10:51:31 AM.
This article is licensed under a Creative Commons Attribution 3.0 Unported Licence.

single-crystalline perovskite photodetectors, *Nat. Commun.*, 2015, **6**, 8724.

21 B. R. Sutherland, A. K. Johnston, A. H. Ip, J. Xu, V. Adinolfi, P. Kanjanaboos and E. H. Sargent, Sensitive, Fast, and Stable Perovskite Photodetectors Exploiting Interface Engineering, *ACS Photonics*, 2015, **2**, 1117–1123.

22 H. Wei, Y. Fang, P. Mulligan, W. Chuirazzi, H. H. Fang, C. Wang and J. Huang, Sensitive X-ray detectors made of methylammonium lead tribromide perovskite single crystals, *Nat. Photonics*, 2016, **10**, 333–339.

23 H. Lu, W. Tian, F. Cao, Y. Ma, B. Gu and L. Li, A Self-Powered and Stable All-Perovskite Photodetector-Solar Cell Nanosystem, *Adv. Funct. Mater.*, 2016, **26**, 1296–1302.

24 Z. Lian, Q. Yan, Q. Lv, Y. Wang, L. Liu, L. Zhang and J. L. Sun, High-Performance Planar-Type Photodetector on (100) Facet of $MAPbI_3$ Single Crystal, *Sci. Rep.*, 2015, **5**, 16563.

25 D. Li, G. Dong, W. Li and L. Wang, High performance organic–inorganic perovskite-optocoupler based on low-voltage and fast response perovskite compound photodetector, *Sci. Rep.*, 2015, **5**, 7902.

26 K. C. Kwon, K. Hong, L. Q. Van, S. Y. Lee, J. Choi, K. B. Kim and H. W. Jang, Inhibition of Ion Migration for Reliable Operation of Organolead Halide Perovskite-Based Metal/Semiconductor/Metal Broadband Photodetectors, *Adv. Funct. Mater.*, 2016, **26**, 4213–4222.

27 X. Hu, X. Zhang, L. Liang, J. Bao, S. Li, W. Yang and Y. Xie, High-Performance Flexible Broadband Photodetector Based on Organolead Halide Perovskite, *Adv. Funct. Mater.*, 2014, **24**, 7373–7380.

28 H. Fang, Q. Li, J. Ding, N. Li, H. Tian, L. Zhang and Q. Yan, A self-powered organolead halide perovskite single crystal photodetector driven by a DVD-based triboelectric nanogenerator, *J. Mater. Chem. C*, 2016, **4**, 630–636.

29 L. Dou, Y. M. Yang, J. You, Z. Hong, W. H. Chang, G. Li and Y. Yang, Solution-processed hybrid perovskite photodetectors with high detectivity, *Nat. Commun.*, 2014, **5**, 5404.

30 J. Chen, S. Zhou, S. Jin, H. Li and T. Zhai, Crystal organometal halide perovskites with promising optoelectronic applications, *J. Mater. Chem. C*, 2016, **4**, 11–27.

31 (*a*) A. Slonopas, B. J. Foley, J. J. Choi and M. C. Gupta, Charge transport in bulk $CH_3NH_3PbI_3$ perovskite, *J. Appl. Phys.*, 2016, **119**, 074101; (*b*) F. F. Masouleh, N. Das and H. R. Mashayekhi, Assessment of amplifying effects of ridges spacing and height on nano-structured MSM photo-detectors, *Opt. Quantum Electron.*, 2014, **47**, 193–201.

32 (*a*) Q. Dong, Y. Fang, Y. Shao, P. Mulligan, J. Qiu, L. Cao and J. Huang, Electron-hole diffusion lengths > 175 μm in solution-grown $CH_3NH_3PbI_3$ single crystals, *Science*, 2015, **347**, 967; (*b*) N. Das, M. F. Fadakar and H. R. Mashayekhi, A Comprehensive Analysis of Plasmonics-Based GaAs MSM-Photodetector for High Bandwidth-Product Responsivity, *Adv. OptoElectron.*, 2013, 1–10.

33 F. F. Masouleh, N. Das and H. R. Mashayekhi, Optimization of light transmission efficiency for nano-grating assisted MSM-PDs by varying physical parameters, *Photonics and Nanostructures*, 2014, **12**, 45–53.

34 F. F. Masouleh, N. Das and S. M. Rozati, Optimal subwavelength design for efficient light trapping in central slit of plasmonics-based metal–semiconductor–metal photodetector, *Opt. Quantum Electron.*, 2015, **47**, 1477–1485.

35 A. Slonopas, B. J. Foley, J. J. Choi and M. C. Gupta, Charge transport in bulk $CH_3NH_3PbI_3$ perovskite, *J. Appl. Phys.*, 2016, **119**, 074101.

36 Q. Dong, Y. Fang, Y. Shao, P. Mulligan, J. Qiu, L. Cao and J. Huang, Electron-hole diffusion lengths > 175 μm in solution-grown $CH_3NH_3PbI_3$ single crystals, *Science*, 2015, **347**, 967.